The Astrophysical Journal, 740:33 (10pp), 2011 October 10 doi:10.1088/0004-637X/740/1/33


# *KEPLER* AND GROUND-BASED TRANSITS OF THE EXO-NEPTUNE HAT-P-11b

Drake Deming[1,6], Pedro V. Sada[2,7], Brian Jackson[1,7,8], Steven W. Peterson[3], Eric Agol[4,5,9], Heather A. Knutson[5,10], Donald E. Jennings[1,7], Flynn Haase[3], and Kevin Bays[3]

[1] Planetary Systems Laboratory, NASA's Goddard Space Flight Center, Greenbelt MD 20771, USA; ddeming@astro.umd.edu
[2] Departamento de Física y Matemáticas, Universidad de Monterrey, Monterrey, Mexico
[3] Kitt Peak National Observatory, National Optical Astronomy Observatory, Tucson, AZ 85719, USA
[4] Department of Astronomy, University of Washington, Seattle, WA 98195, USA
[5] Department of Astronomy, University of California at Berkeley, Berkeley, CA 94720-3411, USA
*Received 2011 April 26; accepted 2011 July 13; published 2011 September 23*

## ABSTRACT

We analyze 26 archival *Kepler* transits of the exo-Neptune HAT-P-11b, supplemented by ground-based transits observed in the blue (*B* band) and near-IR (*J* band). Both the planet and host star are smaller than previously believed; our analysis yields $R_p = 4.31\ R_\oplus \pm 0.06\ R_\oplus$ and $R_s = 0.683\ R_\odot \pm 0.009\ R_\odot$, both about $3\sigma$ smaller than the discovery values. Our ground-based transit data at wavelengths bracketing the *Kepler* bandpass serve to check the wavelength dependence of stellar limb darkening, and the *J*-band transit provides a precise and independent constraint on the transit duration. Both the limb darkening and transit duration from our ground-based data are consistent with the new *Kepler* values for the system parameters. Our smaller radius for the planet implies that its gaseous envelope can be less extensive than previously believed, being very similar to the H–He envelope of GJ 436b and *Kepler*-4b. HAT-P-11 is an active star, and signatures of star spot crossings are ubiquitous in the *Kepler* transit data. We develop and apply a methodology to correct the planetary radius for the presence of both crossed and uncrossed star spots. Star spot crossings are concentrated at phases −0.002 and +0.006. This is consistent with inferences from Rossiter–McLaughlin measurements that the planet transits nearly perpendicular to the stellar equator. We identify the dominant phases of star spot crossings with active latitudes on the star, and infer that the stellar rotational pole is inclined at about $12^\circ \pm 5^\circ$ to the plane of the sky. We point out that precise transit measurements over long durations could in principle allow us to construct a stellar Butterfly diagram to probe the cyclic evolution of magnetic activity on this active K-dwarf star.

*Key words:* planetary systems – planets and satellites: general – stars: activity – starspots

*Online-only material:* color figures

## 1. INTRODUCTION

The exo-Neptune HAT-P-11b (Bakos et al. 2010, hereafter B10) is prominent among extrasolar planets smaller than Saturn. HAT-P-11b transits a bright star ($V = 9.59$) that lies in the *Kepler* field (Borucki et al. 2010). Based on its position in a mass–radius diagram (e.g., Figure 14 of B10), HAT-P-11b is likely to have a massive atmosphere. Moreover, B10 found good mass and radius agreement with metal-rich models for the planet (Baraffe et al. 2008), and the B10 spectroscopic analysis of the host star indicated that it was metal-rich. The planet's atmosphere is therefore likely to exhibit a significant molecular absorption spectrum during transit and/or eclipse. It is a tempting target for future spectroscopic characterization, for example using precise ground-based spectrophotometry (e.g., Bean et al. 2010) in combination with the *Hubble Space Telescope* (*HST;* Pont et al. 2009), and/or warm *Spitzer* (Desert et al. 2011). Prior to such efforts, it is important to improve our current knowledge of the system parameters and optical planetary radius by examining the *Kepler* data.

Based on photometric variations of the star, B10 concluded that star spots were common on the stellar photosphere. Rossiter–McLaughlin (R-M) observations of the system (Winn et al. 2010; Hirano et al. 2011) indicate that the planet's orbital angular momentum vector is nearly perpendicular to the orbital angular momentum vector of the star. Winn et al. (2010) predicted that this misalignment would produce a characteristic signature in the spot-crossing patterns seen during transit, and this should be quite evident in the *Kepler* data.

In this paper, we report an analysis of Q0–Q2 archival *Kepler* data for transits of HAT-P-11b, supplemented with new ground-based transit data at wavelengths bracketing the *Kepler* bandpass. The potential benefits of ground-based transit photometry as a complement to *Kepler* have been emphasized by Colon & Ford (2009).

## 2. OBSERVATIONS AND PHOTOMETRY

### 2.1. Ground-based Observations

We observed a transit of HAT-P-11b from Kitt Peak on UT 2010 June 1, at two wavelengths approximately bracketing the *Kepler* bandpass. For the longer wavelength, we used the 2.1 m reflector with the FLAMINGOS 2048 × 2048 pixel infrared imager (Elston 1998), and a *J*-band (1.25 $\mu$m) filter, at $0\farcs6$ pixel$^{-1}$ scale. Following the conclusion of nightly public programs, we had access to the 0.5 m telescope at the Kitt Peak Visitor Center (VCT). Simultaneously with the 2.1 m *J*-band observations, we observed the same transit at short wavelengths

[6] Current address: Department of Astronomy, University of Maryland at College Park, College Park, MD 20742, USA.
[7] Visiting Astronomer, Kitt Peak National Observatory, National Optical Astronomy Observatory, which is operated by the Association of Universities for Research in Astronomy under cooperative agreement with the National Science Foundation.
[8] NASA Postdoctoral Fellow.
[9] Miller Visiting Professor at UC Berkeley.
[10] Miller Fellow.

using VCT and a 3072 × 2048 CCD camera at 0.″45 pixel$^{-1}$. The VCT observations were acquired in an AstroDon *B*-band filter (390–510 nm). Observations at both telescopes used a defocus to about 10″ in diameter to improve the photometric precision, and both used off-axis guiding to maintain pointing stability. Exposure times were 30 s at the 2.1 m, and 60 s at VCT. All of the optical CCD exposures at VCT were binned 2 × 2 to facilitate rapid readout.

Flat-field observations were acquired using either twilight sky (VCT), or a series of night-sky FLAMINGOS exposures including pointing offsets to allow removal of stars via a median filter.

Our HAT-P-11 transits were observed on the sixth night of a seven-night contiguous run on the 2 m telescope. At the outset of each observing run, we checked the FLAMINGOS instrument clock to be certain that it was synched with GPS time signals. Analyzing the transit data from this 2010 May–June run, we have discovered large (∼300 s) differences, exceeding the random errors, between transit times for other planets measured simultaneously at VCT versus the 2 m. These anomalies occured during the last half of the observing run, and unfortunately the FLAMINGOS instrument clock was not rechecked at the end of the run. Although we have no direct evidence of clock errors, we conservatively regard our observed *J*-band or *B*-band transit times as suspect, and we omit these transit timings from the updated ephemeris described in Section 6. The photometric shapes of our ground-based transit curves are not affected by this issue.

### 2.2. *Photometry on the Ground-based Data*

Subsequent to dark current subtraction and division by a flat-field frame, we performed aperture photometry on the target star and comparison stars. The 20′ field of FLAMINGOS provided six comparison stars of comparable IR brightness to HAT-P-11. We used a circular aperture 31 pixels in diameter (18.″6 diameter, 9.″3 in radius) to measure the stars. We varied the aperture size to optimize the precision in the ratio of HAT-P-11 to the ensemble of comparison stars. We subtracted sky background using an annulus having an inner radius of 18 pixels and an outer radius of 25 pixels. Normalizing HAT-P-11 to the comparison stars yielded a transit light curve with an observed scatter that varied from 0.0016 before transit to 0.0008 after transit due to the decreasing airmass during the observations. The latter precision (0.0008) is comparable to the current best ground-based photometry in the *J* band (e.g., Croll et al. 2011). We estimated an error for each HAT-P-11 *J*-band photometric point as the standard deviation of the ratio to the individual comparison stars, divided by the square root of their number (error of the mean). All of our quoted error and precision values are given as linear ratios to the average intensity value, not as magnitudes.

Our photometric aperture for HAT-P-11 nominally excludes a faint companion (2MASS19505049+4805017) lying 10.″7 north of HAT-P-11. However, because of the defocus, some flux from the companion will fall within the HAT-P-11 aperture. Fortunately, the companion is 6.0 magnitudes fainter than HAT-P-11 at *J*, and 6.2 magnitudes fainter in the optical (*Kepler* magnitude). There is no information available as per possible variability of the companion, but we see no temporal anomalies in our ground-based data (nor in the *Kepler* data for HAT-P-11). The principal known effect of the companion is that the normalizing (out-of-transit) flux for our HAT-P-11 photometry may be overestimated by as much as 1.003. Fortunately, even the maximum contamination will have a negligible effect on our results. Consider an out-of-transit flux equal to $1+\epsilon$, where $\epsilon$ is the contribution of the companion. Let the in-transit flux be $1+\epsilon-\delta$, where $\delta$ is the depth of the uncontaminated transit. The misnormalized in-transit flux is therefore $(1+\epsilon-\delta)/(1+\epsilon) \approx 1-\delta+\epsilon\delta$. In the case of HAT-P-11 we have $\delta \approx 0.004$, and possible contamination $\epsilon \approx 0.003$. The second-order term will affect no more than ±1 in the least significant digit of our results, even for our *Kepler* analysis (see below). We therefore ignore possible contamination from 2MASS19505049+4805017.

After normalizing to the comparison stars, the HAT-P-11 *J*-band photometry exhibited low-amplitude (0.0005) parabolic curvature in the out-of-transit baseline. It is probable that this baseline curvature is caused by differences in the effective wavelengths of the *J* bandpass as a function of stellar color, in combination with the wavelength variation in telluric water vapor absorption. This is a familiar effect that we have seen in other *J*-band photometry (Sada et al. 2010). We removed this baseline curvature using a second-order polynominal fit, masking off the in-transit portion. Because the baseline intensity varies slowly with wavelength, it does not affect the point-to-point scatter in the transit curve. However, baseline uncertainty does represent a potential source of systematic error for the transit depth, as discussed in Section 8.

Photometry of the VCT *B*-band data used similar procedures as those for the FLAMINGOS *J*-band data, except that only two comparison stars were usable, but no quadratic baseline correction was needed. Figure 1 shows our ground-based transit data for both bands, in comparison to transit curves calculated using the analytic relations of Mandel & Agol (2002), with the B10 system parameters, and limb-darkening coefficients from Kurucz model atmospheres (see Section 4).

## 3. *KEPLER* OBSERVATIONS

We analyzed public archival data for HAT-P-11 in quarters Q0–Q2. Our analysis uses the short cadence (Gilliland et al. 2010) Pre-search Data Conditioned (PDC) light curves from the Multimission Archive at STScI (Space Telescope Science Institute) archive. We remove outlying photometric points from the light curves using a 4$\sigma$ clip applied to the difference between the PDC light curve and a five-cadence median of that same light curve. The brightness of HAT-P-11 varies slowly due to the rotation of star spots with a 29 day period (B10). In principle, this brightness variation could be exploited to correct for the presence of those spots (Czesla et al. 2009). However, the particular circumstance of the HAT-P-11b transit motivates a better method to implement a star spot correction (explained below). We therefore remove and discard the stellar brightness variations that bracket each transit. We isolate a section of light curve spanning the center of each transit by ±2.3 hr. Masking off the transit, we fit a straight line to the stellar variation over that section, and find the ratio of the transit light curve to the straight line.

We here verify that a straight line adequately represents the stellar rotational variability over the 4.6 hr duration of each transit event. As part of our investigation into the noise properties of the data (see below), we fit straight lines to 4.6 hr sections of the data centered on arbitrary planetary orbital phases where no transit or eclipse occurs. Because any residual curvature could vary from convex to concave, we average the absolute value of the deviations from each fitted straight line. We fit a parabola to the average of those absolute deviations. We repeat this test for 14 different phases in the planetary orbit,

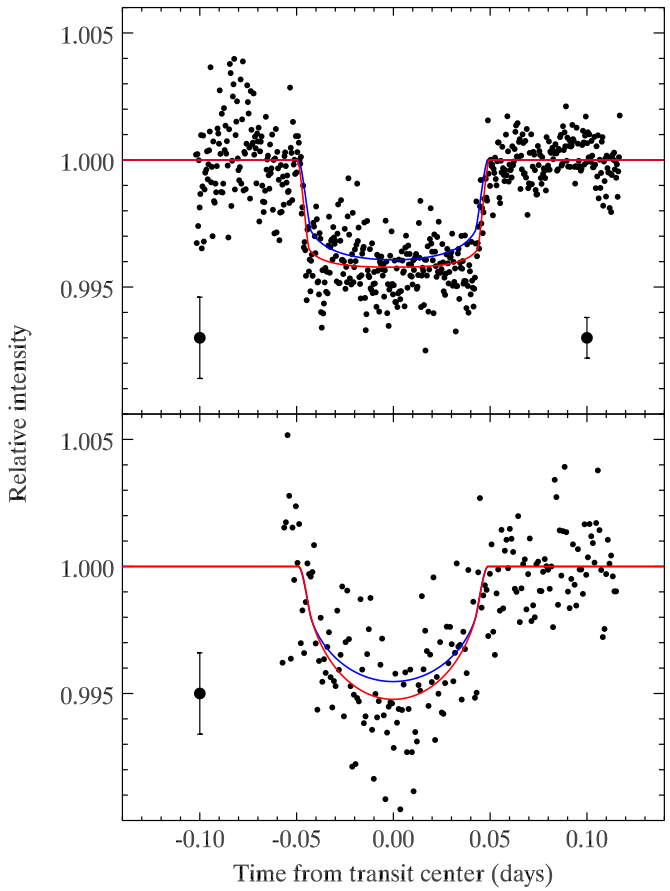


**Figure 1.** Transit of HAT-P-11 observed in the *J* band (upper panel) and *B* band (lower panel) from Kitt Peak on 2010 June 1. A quadratic baseline has been removed from the *J*-band photometry, as noted in the text. The error bars per point are indicated by the inset points; for the *J*-band observations the error bars decreased after transit due to decreasing airmass. The overplotted blue curves are the nominal transit shapes expected using the system parameters from Bakos et al. (2010) and limb darkening from a Kurucz model atmosphere. Note that the observed duration of transit for the *J* band is greater than expected from the blue curve. The red curves are based on our best-fit parameters from Table 1.

(A color version of this figure is available in the online journal.)

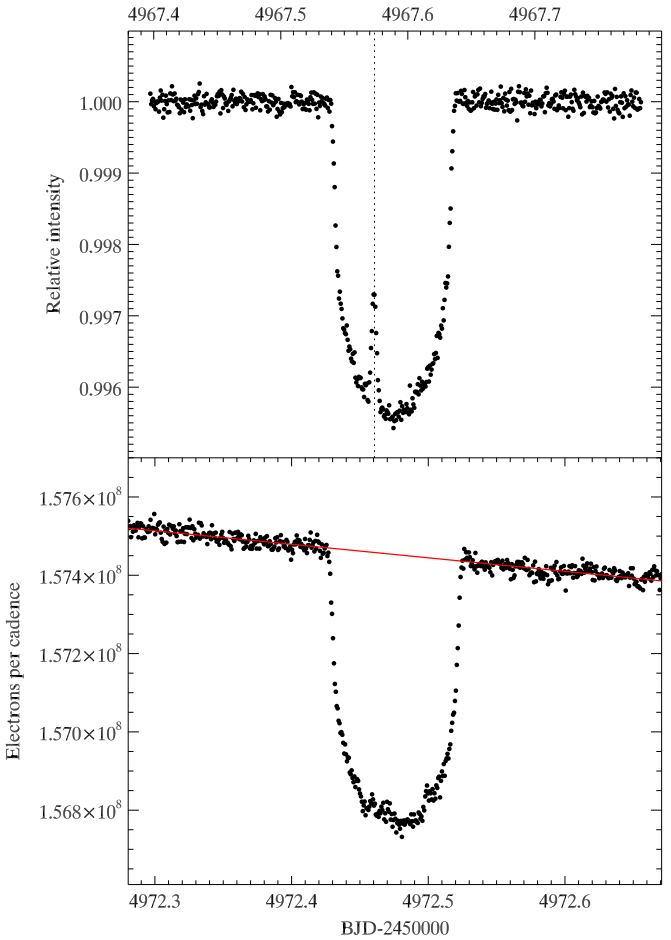


**Figure 2.** Upper panel: detrended and normalized transit of HAT-P-11 observed by *Kepler* on 2009 May 15. The vertical dashed line marks a prominent effect due to a star spot crossing. Lower panel: the next successive transit observed by *Kepler* following the May 15 transit, shown before normalization and trend removal. The red line is the variability of the star, taken to be linear over the span of the transit.

(A color version of this figure is available in the online journal.)

avoiding the transit itself. In the worst of the 14 cases, the maximum span of that parabola over 4.6 hr is less than four parts per million (ppm), and baseline excursions of that magnitude will have negligible impact on our analysis. The fact that the planetary orbit is not phased to the stellar rotation period implies that baseline effects from stellar rotation will be further reduced when stacking multiple transits. We conclude that straight line baselines are adequate for extracting transits of the planet over 4.6 hr sections of the *Kepler* data. Figure 2 shows an example of a transit with the linear baseline removed, as well as an additional transit illustrated at the stage prior to removal of the linear baseline.

### *3.1. Noise Properties of the Kepler Data*

Our results for HAT-P-11 are heavily dependent on the *Kepler* data, so it is prudent to investigate the noise properties of these data, especially in the limit in which they are averaged to achieve very high photometric precision. By noise properties, we mean not only the low-amplitude artifacts inherent in the data themselves (Gilliland et al. 2010), but also the existence of fluctuations caused by stellar activity, such as low-amplitude flares (Walkowicz et al. 2011). A conventional method for evaluating the noise properties of photometric data is to measure the standard deviation of binned data as a function of the number of points that are binned. For stationary white noise, we expect that the standard deviation of fluctuations about a mean value will decrease as the inverse square root of the number of binned points. Standard deviations greater than this scaling law are attributed to the so-called red noise (Pont et al. 2006).

To investigate the noise properties of the *Kepler* data, we perform both a conventional binning test and a more specialized test. Both tests begin by extracting twenty-six 4.6 hr sections of the data centered at an arbitrary phase, i.e., *not* centered on transit or secondary eclipse. We fit and remove a straight line to each of these data sections and bin the residuals in two ways. First, we bin consecutive points in each section, compute the standard deviation of the binned data, and average the standard deviations over the 26 sections. Second, we bin the data non-consecutively, by combining points from different sections into a common phase bin whose width is approximately one cadence (60 s, 0.00015 in phase). Figure 3 shows the results from both binning procedures. The standard deviation for consecutive binning decreases as $N^{-0.34}$, indicating the presence of red noise in the data. However, the standard deviation for non-consecutive binning agrees very precisely with the $N^{-0.5}$ relation, indicating that noise components do not persist at a specific phase from one

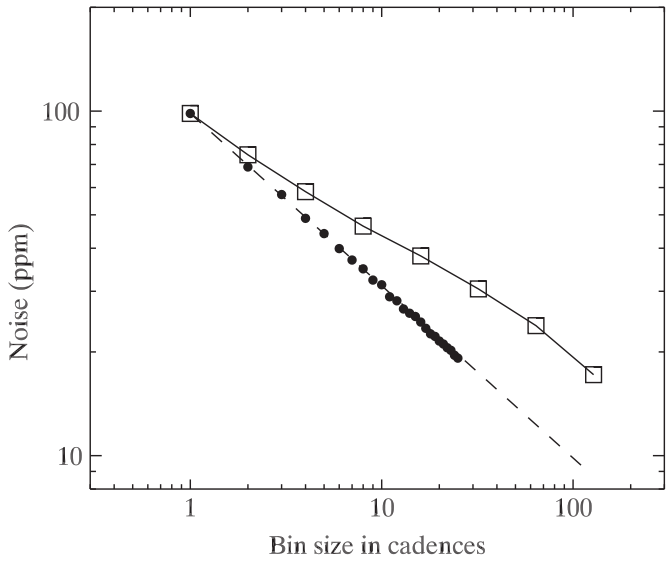


**Figure 3.** Noise properties of the HAT-P-11 short cadence data, showing standard deviation (ordinate, in parts per million) of binned data vs. bin size (abscissa). The open squares are for binning consecutive data points and lie above the theoretical relation (dashed line) due to correlated red noise of low amplitude. The solid points show noise amplitudes from bins at a given phase, constructed from $N$ 4.6 hr sections of data, vs. $N$. These points lie almost exactly on the theoretical relation (dashed line), showing that noise is uncorrelated from one orbit of HAT-P-11 to another.

orbital period to another. Our procedure for combining transits (see below) shifts them to a common phase, i.e., we use non-consecutive binning. Although red noise in the data will increase the scatter for each individual transit, the noise in the phased and averaged transit decreases as $N^{-0.5}$, where $N$ is the number of points in each bin of the combined transit.

### 3.2. Removal of Transited Star Spots

Our analysis includes 26 transits of HAT-P-11 from the *Kepler* data and *all* of them show signs of star spot crossings, albeit less prominently than the Figure 2 example. We have corrected these HAT-P-11b transits for the presence of spots crossed by the planet as well as spots *not* crossed by the planet. We here describe the correction for crossed spots; the uncrossed spot correction we defer to Section 7.

Our correction methodology for crossed spots begins by combining the 26 transits, i.e., transforming them to a common time frame. In so doing, we must minimize interference by the crossed spots to our process of time-shifting the transits. We note that the effect of star spots will be greatly reduced at ingress and egress by two favorable factors. First, spots during ingress and egress will be foreshortened by the limb-viewing geometry. Second, we expect few spots to occur at ingress and egress due to the nature of star spot distributions. The R-M results (Winn et al. 2010; Hirano et al. 2011) indicate a large angle between the stellar equator and the planetary orbital plane. Hence, ingress and egress will probably occur near the poles of the star. We expect few star spots at the stellar poles, analogous to our Sun, but we acknowledge that polar spots do occur on some active stars (Waite et al. 2011).

To exploit these favorable factors, we use the ingress and egress data to determine the center of temporal symmetry for each transit by constructing bisectors of the transit curve at six intensity levels: 0.9995, 0.9990, 0.9985, 0.9980, 0.9975, and 0.9970. We average those bisectors to obtain the temporal center

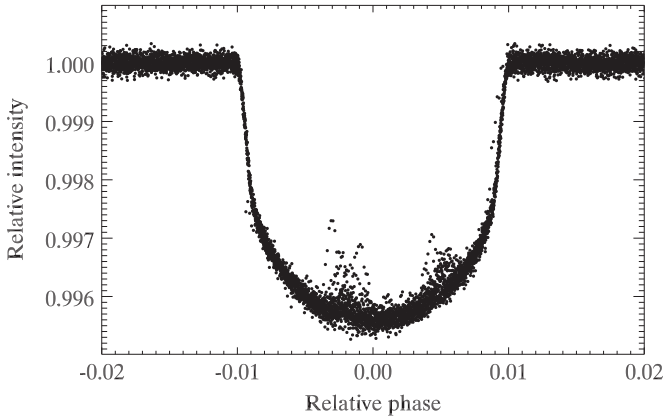


**Figure 4.** Stack of 26 detrended and normalized transits of HAT-P-11 from the *Kepler* Q0–Q2 data. Note the tendency of perturbations by star spot crossings to concentrate at orbital phases near −0.002 and 0.006. We attribute this to crossings of active latitudes by the planet in a highly inclined orbit (Winn et al. 2010; Hirano et al. 2011).

of symmetry for each transit. We use those temporal centers to compute an updated ephemeris for the planet (Section 6). The deviation of individual transits from the new ephemeris is typically about 10 s, with no evidence for genuine timing variations. We therefore use the new ephemeris to combine the transits onto a common time frame. This combined transit is shown in Figure 4, with the abscissa expressed as orbital phase relative to transit center.

Active regions on our Sun are known to concentrate at "active latitudes" (sometimes called "preferred latitudes") located symmetrically about the solar equator. Figure 4 shows that the effect of HAT-P-11b's star spot crossings cluster at two orbital phases (−0.002 and 0.006), which we interpret as the planet crossing's two active latitudes. This view is consistent with the expected distribution of star spots as well as the R-M results (Winn et al. 2010; Hirano et al. 2011) that indicate that the planet is orbiting nearly perpendicular to the plane of the stellar rotational equator. Under the assumption that the active latitudes are located symmetrically about the stellar rotational equator, we find that the planet crosses the stellar equator at phase 0.002. This implies that the angle between the plane of the sky and the stellar rotational axis is approximately $12^\circ \pm 5^\circ$, where we estimate the precision from the phase scatter of the two active latitude crossings.

To remove the effect of the active latitude crossings, we exploit gaps in the longitudinal distribution of the star spots. If spots completely covered the active latitudes on the star, the signatures of spot crossings would appear every time the planet crossed an active latitude. However, analogous to our Sun, we expect significant gaps between spots on an active latitude. Thus, spot crossings only occur when the planet crosses an active latitude and the longitude of the planet and a star spot coincide. Moreover, Figure 4 implies that active latitudes are broad: the phase (hence latitude) distribution of crossed spots in a given hemisphere is not single-valued. We therefore proceed to remove the effect of crossed spots as follows. First, we group the Figure 4 data using two bin sizes. During the transit (first to fourth contacts), we use a bin width of 0.00015 in phase (1 minute, about the same as the *Kepler* short cadence time). Keeping the bin width short will eliminate significant distortion of the transit curve shape (Kipping 2010). Out of transit, we bin the stellar continuum with a bin width of 0.0006 in phase (4.2 minutes).

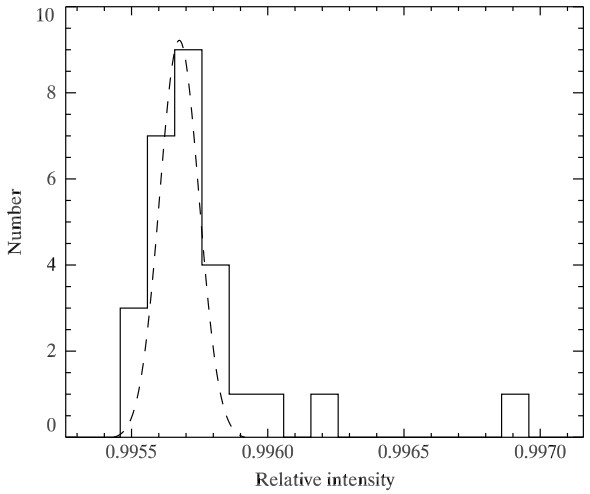


**Figure 5.** Example of star spot removal at one particular phase in the stacked HAT-P-11 transits of Figure 4. The dashed line is a fit of a Gaussian to the histogram of relative intensities at (in this example) phase −0.00098. The center of the Gaussian fit at intensity 0.99567 is the value of the transit curve at this phase with star spot crossings removed.

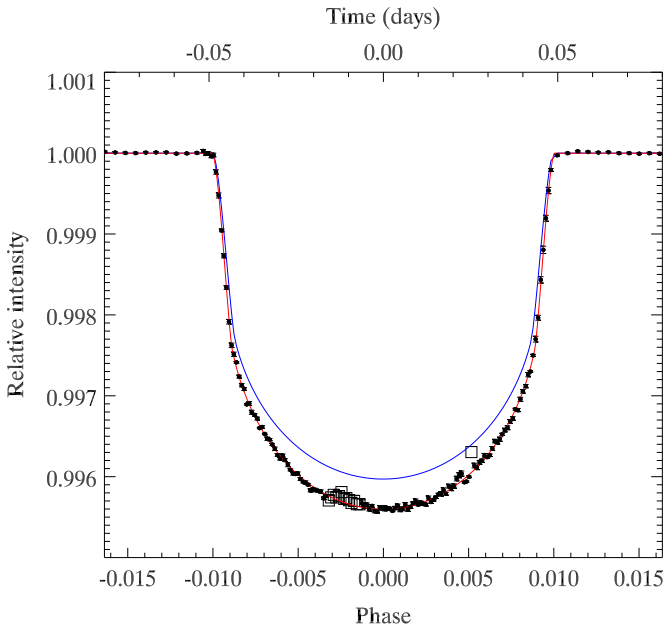


**Figure 6.** Average *Kepler* transit curve for HAT-P-11, based on removing star spot crossings and averaging the Figure 4 data. The red line is our best-fit MCMC solution (*Kepler*-1 line in Table 1). Error bars for these *Kepler* data are plotted, but are difficult to discern, being comparable to the size of the plot symbols. The square points near phase −0.0025 and the single point at +0.0055 were zero-weighted in the fit. The blue curve is the transit expected using the B10 system parameters, with the *Kepler*-1 limb-darkening coefficients (Table 1).
(A color version of this figure is available in the online journal.)

For each phase bin, we construct a histogram of relative intensities within that bin, and we fit a Gaussian to the peak of that histogram. The spot-corrected intensity for the transit curve at that phase is taken as the centroid of the Gaussian. To ensure that peaks in the wings of the histogram do not perturb the Gaussian fit to the main peak, we do the fitting iteratively. Following a preliminary Gaussian fit, we zero those portions of the histogram lying more than $2.5\sigma$ distant from the Gaussian center, then we re-fit to the main peak. The assumption underlying this method is that star spots are only a perturbation to the dominant intensity at a given phase, and that the most common intensity observed at that phase is not affected directly by star spots. If this assumption were not valid, then all methods that do not interpolate over the spot-crossing region from other phases would fail. In that sense our underlying assumption is no more restrictive than nature itself. Some of the low-lying points in Figure 4 could be due to bright active-region morphology, such as plage. Our methodology automatically corrects for plage perturbations as well as spots. Figure 5 shows an example of our histogram prior to zeroing the wings, with the Gaussian fit to the peak.

Figure 6 shows the result of binning and spot-correcting the stacked transits from Figure 3. The effects of transited star spots are largely eliminated in the Figure 6 transit curve, except for a group of noisy points near phase −0.0025, and a single outlying point near phase +0.0055. The spot correction is imperfect in the sense that the scatter over much of the in-transit portion is about twice that expected from *Kepler*'s photometric precision. Nevertheless, this combined transit is much less affected by spot crossings than the individual transit curves. We note that our correction method is fundamentally statistical in nature, and will produce even better results as additional *Kepler* transits of this system become available.

## 4. LIMB DARKENING

Prior to fitting the ground-based and *Kepler* data to derive improved system parameters, it is necessary to consider the effect of stellar limb darkening. In fitting to *Kepler* data for TrES-2, Kipping & Bakos (2011) pointed out that adopting limb-darkening coefficients from model atmospheres can potentially make the transit results model-dependent to an undesirable degree. We have therefore used both approaches, adopting limb-darkening coefficients from a Kurucz model atmosphere for HAT-P-11, as well as fitting for them.

B10 inferred stellar parameters for HAT-P-11 of 4500/4.5/0.3 in Teff/log $g$/[Fe/H]. We used a Kurucz model atmosphere with parameters 4500/4.5/0.5,[11] because the Kurucz grid is tabulated at 0.5 increments in metallicity. We verified, by comparison with a solar metallicity model, that the difference between metallicity +0.3 and +0.5 will be negligible for limb darkening. At each of 17 disk positions ($\mu$-values), we weighted the model atmosphere intensities by the filter or *Kepler* bandpass functions, and integrated over wavelength. This defined the limb darkening for each bandpass.

We fitted linear and quadratic coefficients for the standard expressions to the results of our model atmosphere integrations (Claret et al. 1995). Sing (2010) has calculated limb-darkening coefficients for the *Kepler* bandpass, and we compared our results to his tabulation. For 4500/4.5/0.5, we find (linear, quadratic) coefficients of (0.6136, 0.1062) versus (0.6266, 0.1057) for Sing (2010). We performed similar calculations for the $J$- and $B$-band filter functions. Comparing our quadratic coefficients to Claret et al. (1995) for the $J$-band filter and 4500/4.5/0.5, we find reasonable agreement: (0.290, 0.244) for us and (0.267, 0.255) from Claret et al. (1995). For the $B$-band filter, we find that the Kurucz limb darkening can be well approximated using linear limb darkening, i.e., with the quadratic coefficient set to zero.

We conclude that our calculation of limb-darkening coefficients accurately reflects the output of Kurucz model atmospheres. But whether the actual star conforms to those

[11] http://kurucz.harvard.edu/grids/gridP05.

calculations must be determined by comparison to our transit data.

## 5. TRANSIT-FITTING METHODOLOGY

### 5.1. Priors and Transit Curves

The orbit of HAT-P-11 has non-zero eccentricity ($e = 0.198$, B10). In principle, precise transit light curves may reveal some direct signature of a non-zero eccentricity such as acceleration between ingress and egress. However, detection of the secondary eclipse (e.g., using *Spitzer* photometry) is potentially the most sensitive constraint on the eccentricity of the orbit (Charbonneau et al. 2005; Deming et al. 2005). *Spitzer* observations of HAT-P-11 spanning the time of secondary eclipse were obtained by R. Barry (*Spitzer* program 60063), but those data are still under analysis. Indeed, it is possible that the secondary eclipse of this relatively cool planet will prove too weak to be detectable in the *Spitzer* data. Therefore, for all of our transit fits, we fix the orbital eccentricity and argument of periastron at the values derived by B10, except that we alter $\omega$ by 180°, as per the difference between $\omega$ for radial velocity observations (orbit of the star) and $\omega$ for transits (orbit of the planet).

We compute transit curves using a new version of the Mandel & Agol (2002) algorithms. This new version includes the effects of a non-circular orbit, calculating the sky-projected distance of the planet from the center of the stellar disk by solving the elliptical geometry. We also specifically verified that our code can reproduce the observed radial velocities for this system (B10; Hirano et al. 2011; Winn et al. 2010). The new code is also faster than previous versions.

### 5.2. Markov Chain Monte Carlo Code

We fit theoretical transit curves to the transit data using a Markov Chain Monte Carlo (MCMC) algorithm (Ford 2005). We use the Metropolis–Hastings algorithm with Gibbs sampling. We adjust the step size for each variable so as to obtain acceptance rates between 30% and 60%, and we run our chains for $10^6$ samples. Prior to starting each MCMC chain, we re-scale the error bars for the data to ensure that the best reduced $\chi^2$ will be close to unity. This helps to ensure that the errors calculated from the posterior distributions are realistic. The re-scaling factor was approximately two for the binned *Kepler* data. For the ground-based data, we adopt error bars equal to the observed scatter in the data, so no re-scaling is necessary.

We discard the first 20% of each chain when tabulating the posterior distributions. To verify convergence, we compare the posterior distributions from four chains that have different starting values and slightly different step sizes. Since our code is new, we tested it in several ways. These tests began with simple numerical problems such as fitting to an average of a series of numbers, and fitting to data that scatter around a straight line. Our final test was to generate synthetic transit data by adding noise to theoretical transit curves based on the Mandel & Agol (2002) formulae, and fitting to those synthetic transits to verify that we recover the system parameters that were used to generate the synthetic data.

### 5.3. Kepler Transit Fits

Ideally, we would like fit to all of the individual transit curves simultaneously, allowing the central transit times to be free parameters in the fit. However, the spot crossings that contaminate individual transits force us to fit to the binned and cleaned transit (Figure 6). One caveat to this procedure is that imperfections in the mutual phasings of the transits could potentially broaden and distort the binned transit. To check our result, we combined the transits in two ways. First, we used our new ephemeris (Section 6) to shift each transit to a common phase. Second, we used the raw individual central transit times from the bisector analyses to phase the transits. We performed all of our MCMC fits to binned transits constructed using both methods, and found agreement within the random errors. We are confident that phasing errors do not contaminate our results to a significant degree. We report the fit results from the ephemeris phasing because it employs the constraint that the transit times should be strictly periodic in the absence of planetary perturbations.

Our MCMC fits to the binned and cleaned *Kepler* data (Figure 6) included six variables in the fit: $a/R_s$, $R_p/R_s$, orbital inclination, quadratic and linear limb-darkening coefficients, and a correction to transit center time. The last variable is expected to be zero because the stacking and binning procedures aligned the individual *Kepler* transits to the common transit-centered time frame. Within the errors, the MCMC fits retrieved a central time correction consistent with zero. We performed a second independent set of MCMC fits to the *Kepler* data by fixing the limb-darkening coefficients at their model-atmosphere values.

We tabulated best-fit values for the system parameters by averaging over the last 800,000 samples for four independent MCMC chains. As a check on those best-fit values, we implemented an independent $\chi^2$ minimization solution using a Levenberg–Marquardt algorithm. Our $\pm 1\sigma$ error limits equal the values where high and low-side tails of the MCMC posterior distributions contained 15.9% of the total samples. The error limits were close to symmetric on each side of the distributions (high- and low-side errors typically agree within 10%). We conservatively adopt the greater value as the symmetric error for each fitted parameter. The best-fit values and errors are listed in Table 1, except for the quadratic limb-darkening coefficient that has little impact on our analysis. The best-fit transit curve is plotted over the binned transit data in Figure 6, together with the curve expected from the B10 discovery parameters.

**Table 1**
Results of MCMC Fitting to HAT-P-11b Transits

| Band and Methodology | $u$ | $i$ | $R_p/R_s$ | $a/R_s$ |
|---|---|---|---|---|
| *Kepler*-1 | 0.626 | 89.41 | 0.05892 | 16.549 |
| ··· | ±0.014 | ±0.37 | ±0.00027 | ±0.230 |
| *Kepler*-2 | 0.6179 | 89.58 | 0.05865 | 16.574 |
| ··· | ··· | ±0.28 | ±0.00017 | ±0.156 |
| *J* band | 0.086 | 89.41 | 0.06274 | 16.454 |
| ··· | ±0.065 | ··· | ±0.00066 | ±0.131 |
| *B* band | 1.000 | 89.41 | 0.0596 | 16.549 |
| ··· | ±0.080 | ··· | ±0.0011 | ··· |

**Notes.** *Kepler*-1 and *Kepler*-2 refer to different treatment of limb darkening. The *Kepler*-1 line is our preferred solution; it fits to the linear ($u$) and quadratic limb-darkening coefficients, whereas the *Kepler*-2 solution holds both $u$ and the quadratic coefficient fixed at their Kurucz model atmosphere values (see the text). Both the *J*-band and *B*-band solutions hold the inclination fixed at the *Kepler*-1 value, and the *B*-band solution also holds $a/R_s$ fixed at the *Kepler*-1 value.

### 5.4. J- and B-band Transit Fits

The ground-based data give us an opportunity to check parameters such as limb darkening over an extended wavelength range.

**Table 2**
HAT-P-11b Transit Times ($T_c$) from *Kepler* Data

| $N$ | $T_c$ (BJD-2450000) | Error ($1\sigma$) |
|---|---|---|
| 72 | 4957.81318 | 0.00007 |
| 73 | 4962.70114 | 0.00010 |
| 74 | 4967.58897 | 0.00007 |
| 75 | 4972.47667 | 0.00013 |
| 76 | 4977.36448 | 0.00007 |
| 77 | 4982.25215 | 0.00010 |
| 78 | 4987.14006 | 0.00011 |
| 79 | 4992.02769 | 0.00008 |
| 80 | 4996.91569 | 0.00008 |
| 82 | 5006.69137 | 0.00012 |
| 83 | 5011.57889 | 0.00015 |
| 85 | 5021.35458 | 0.00012 |
| 86 | 5026.24279 | 0.00011 |
| 87 | 5031.13042 | 0.00014 |
| 89 | 5040.90599 | 0.00012 |
| 90 | 5045.79376 | 0.00007 |
| 91 | 5050.68135 | 0.00007 |
| 92 | 5055.56929 | 0.00009 |
| 93 | 5060.45709 | 0.00012 |
| 94 | 5065.34506 | 0.00011 |
| 95 | 5070.23280 | 0.00007 |
| 96 | 5075.12061 | 0.00007 |
| 97 | 5080.00832 | 0.00007 |
| 98 | 5084.89609 | 0.00007 |
| 99 | 5089.78421 | 0.00014 |

**Notes.** Times are TDB (Eastman et al. 2010), and our best-fit ephemeris, with the ground-based transits included, is $T_c = 2454605.89155 + 4.8878018N$, as given in Section 6.

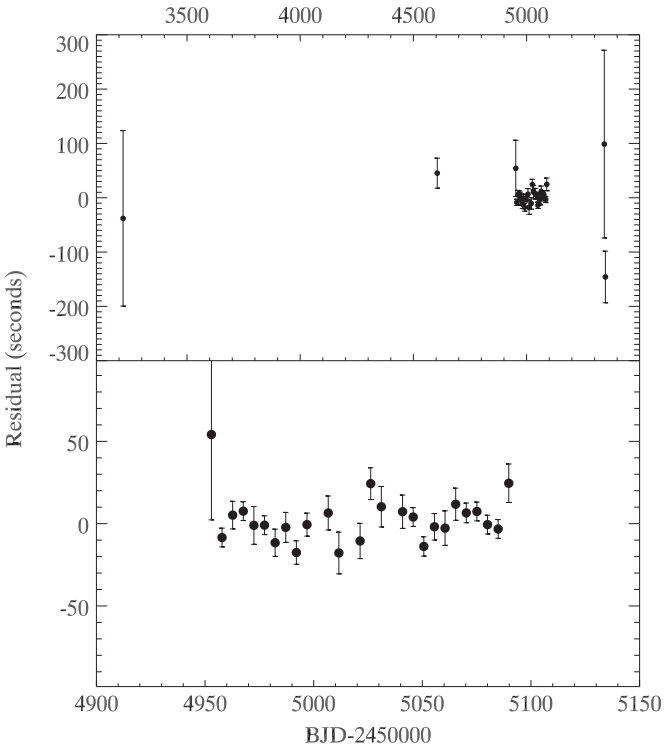


**Figure 7.** Transit time residuals for HAT-P-11 after removing the best-fit ephemeris described in Section 6. The top panel shows all data; the two rightmost points are from our ground-based data, and they are not included in the ephemeris solution as noted in Section 2.1. The cluster of points near $BJD = 2455000$ are the *Kepler* transits; they dominate the ephemeris solution, and that time interval is expanded in the lower panel.

Moreover, the greatly reduced limb darkening in the $J$-band results in sharp ingress and egress times, and that sharp definition of the transit duration will prove to be useful, as we discuss in Section 8, and as Colon & Ford (2009) predicted. However, because the ground-based data do not have photometric precision comparable to the *Kepler* data, we find it prudent to restrict the ground-based fits to extract fewer parameters. For the $J$ band, we set the quadratic limb-darkening coefficient to equal the model atmosphere prediction (0.244), and we set the $B$-band quadratic coefficient to zero as noted above. Anticipating our results, we find rough agreement between the fits and the model atmosphere limb-darkening predictions. The quadratic portion of the limb darkening has a minor effect compared to the linear coefficient, especially in the $B$ band where the strong limb darkening is well approximated by the linear law. Note that Southworth (2008) found linear limb darkening to be adequate for the analysis of high-quality ground-based transit observations. We judge that we lose little information by our adopted restrictions, but the subsequent restriction in the fitted parameters helps to increase the usefulness of the ground-based data.

In the case of the $B$-band transit data, we are primarily interested in the consistency between the retrieved linear limb-darkening coefficient and the model atmosphere prediction. So in that case, we fix both the orbital inclination and the value of $a/R_s$ to their best-fit *Kepler* values, and we fit only for the linear limb-darkening coefficient, as well as $R_p/R_s$ and central transit time. As regards the linear limb-darkening coefficient, we impose the restriction that the MCMC chains cannot step to values exceeding unity, since those values produce unphysical (negative) disk intensities.

Our first exploratory MCMC chains for the $J$-band fit showed a strong degeneracy between orbital inclination and $a/R_s$. This is not surprising since we have previously highlighted this degeneracy for small planets (Sada et al. 2010). In the limit of a small planet transiting a uniform stellar disk, the transit curve approaches an inverse square-wave function where the duration of the transit measures only the total length of the chord across the stellar disk. In that case, the impact parameter (i.e., orbital inclination) and stellar radius can trade off freely. Hence, in the $J$ band we fix the orbital inclination at the *Kepler* value (89.°41, Table 1), and we solve for $a/R_s$.

Results from the $J$- and $B$-band fit procedures are included in Table 1, and best-fit transit curves are overplotted in Figure 1.

## 6. UPDATED TRANSIT EPHEMERIS

A useful by-product of our transit analyses is that we can update the transit ephemeris for this system. We include transits at the two epochs reported by B10, as well as transits from Hirano et al. (2011) and Dittmann et al. (2009), and the *Kepler* transits. Table 2 gives the central transit times and errors for the *Kepler* transits, using our bisector method. The precision of the updated ephemeris is dominated by the *Kepler* transits, each having a timing precision of the order of 10 s. An error-weighted linear least-squares solution for the ephemeris yields $T_0 = 2454605.89155 \pm 0.00013$, in a barycentric dynamical time (TDB) frame (Eastman et al. 2010), and $P = 4.8878018 \pm 1.6 \times 10^{-6}$ days. We consider this to be a provisional update because many additional values for transit center times will be possible with future *Kepler* data. Figure 7 shows residuals for the times of individual transits, after removing the best-fit ephemeris. As noted in Section 2.1, we omit our 2010 $J$- and $B$-band transits from the

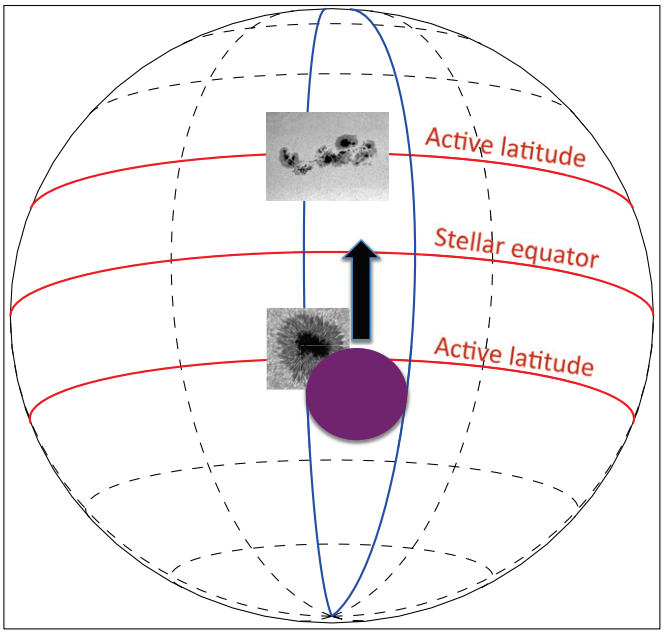


**Figure 8.** Schematic of the HAT-P-11 transit geometry, illustrating that the planet transits nearly perpendicular to the stellar equator, along the sub-Earth longitude of the star. The two blue meridians illustrate that star spot regions crossed by the planet are approximately bounded within a range of longitude (but not to exact scale in this figure). For clarity of the Section 7 discussion, the path of the planet is here illustrated to be perpendicular to the stellar equator. While a perpendicular path is within the error limits of the R-M results, we note that the sky-projected path is nominally tilted by 103° to the stellar equator (Winn et al. 2010).

(A color version of this figure is available in the online journal.)

ephemeris solution, but we include their residuals in Figure 7, where they individually lie off the best-fit ephemeris, but agree with it on average.

## 7. CORRECTION FOR UNCROSSED STAR SPOTS

In the case where multiple high-quality transit light curves are available for a planet that transits at an oblique angle to the stellar equator, we can correct the derived planetary radius for the effect of star spots that are *not* crossed by the planet during transit. The method we describe here assumes that the distribution of star spots is not correlated with the transits. We argue that this method has advantages over inferences based on the rotational light curve of the star (Czesla et al. 2009) because star spot effects in the rotational light curve can be reduced when multiple spots are distributed uniformly over longitude.

The formalism of our star spot correction has two broad steps. First, we integrate over the path crossed by the planet, and average over all observed transits, to calculate the average flux deficit due to star spots on the path of the planet. The orbit of HAT-P-11b is essentially perpendicular (within the errors) to the stellar equator (Winn et al. 2010; Hirano et al. 2011). We find (Table 1) that the orbital inclination is very close to 90°, and therefore the impact parameter is near zero. Moreover, the stellar active latitudes are not far from the stellar equator. Therefore, the flux deficit that we calculate in this first step will be characteristic of regions near the center of the stellar disk. The second broad step will extend the flux deficit calculated over the transit path of the planet, to estimate the total spot coverage over the entire Earth-facing hemisphere of the star.

Figure 8 shows a schematic of the transit geometry. Near disk center, the planet subtends an approximately constant range of longitude as it transits (indicated by blue meridians of longitude in Figure 8). This approximation of course breaks down near the poles because meridians of longitude converge, but we expect few, if any, star spots at the poles. Hence, by integrating over the path of the planet we are essentially defining the spot coverage in the range of longitude defined by the angular extent of the planet.

Consider a highly simplified situation where the planet transits a very small star spot present on a star without limb darkening. Let $F_0$ be the flux from the *unspotted* star, and let $\delta F$ be the stellar flux deficit caused by the small star spot. In transit, before the star spot is crossed, the observed flux $F_{\rm obs}$ is $F_0 - F_0(R_p^2/R_s^2) - \delta F$, where $R_p$ and $R_s$ are the radii of the planet and the star, respectively. When the planet crosses the star spot, the $\delta F$ term vanishes, so the flux becomes $F_{\rm obs} = F_0(1 - R_p^2/R_s^2)$, which is the usual expression for the in-transit flux of a star neglecting limb darkening. The effect of the star spot will be seen in the transit curve as an inverted square wave of amplitude $\delta F$, lasting for a crossing time (measured in phase units) $t_\phi$. (Note that we use orbital phase as a time variable, not an angle.)

A very small star spot would create a simple square-wave-type signature in the transit curve, but real star spots are comparable to the size of the planet itself, their intensity varies from the outer penumbra to their umbral core, and they often occur in groups. Therefore, their signature in transit light curves can be complex, not a simple square wave. Nevertheless, we can derive the total star spot flux deficit crossed by the planet during a transit, $\delta F_t$, as

$$\delta F_t = \int \delta F(\phi) d\phi / t_\phi,$$

where $\delta F(\phi)$ is the amplitude of the deviation seen in the transit curve at phase $\phi$, and the integral is taken over the path of the planet, literally over the transit curve. We need not explicitly consider the intensity gradient across a star spot; we can derive the total flux deficit from the above integral, independent of star spot morphology. Moreover, we can evaluate the integral directly from the observed transit curves; we use the stacked transit curves (Figure 4). We also calculate that $t_\phi = 0.785D/vP = 0.000997$, where $v$ is the tangential velocity of the planet in its orbit, $P$ is orbital period, and $D$ is the planet's diameter. The factor of 0.785 allows for the fact that the average chord across a circular planet is less than the diameter. The numerical integration of the Figure 4 transits yields $\delta F_t = 0.001037$ in flux units where $F_{\rm obs} = 1$. This value applies to the flux deficit over a range of longitudes defined by the angular extent of the planet at disk center (between the two blue meridians in Figure 8). Over that longitude range, the total flux deficit due to star spots is (on average) about 0.1%. Because $2R_p/R_s \approx 0.118$, the 0.1% applies to a range of about 0.118 radians. There are 26 such wedges of longitude on the entire Earth-facing hemisphere of the star. Neglecting limb effects, the total star spot flux deficit could be as large as 2.7%.

Our second broad step assumes that the average size and abundance of star spots is independent of disk position, but that the projected area—hence the flux deficit—of star spots decreases as $\cos\theta$, where $\theta$ is the angular longitude distance from disk center. Our second step will therefore integrate over longitude ($\theta$) to obtain the total flux deficit for the entire Earth-facing hemisphere of the star. Thus,

$$F_0 = F_{\rm obs} + \int_{-\pi/2}^{\pi/2} \delta F_t \theta_p{}^{-1} \cos(\theta) d\theta = F_{\rm obs} + 2\delta F_t/\theta_p,$$

where $\theta_p$ is the longitude interval covered by the planet during transit. This integration yields $F_0 = 1.0176 F_{\rm obs}$. So we calculate that the star spots on HAT-P-11 cause the observed stellar flux to be, on average, lower by 1.76% compared with an unspotted star of the same radius and spectral type. The peak-to-peak variations seen in the stellar rotational light curve are about 1.5% in the *Kepler* data. This is somewhat smaller than 1.76% because the broad distribution of the spots in longitude reduces their signature in the rotational light curve. We note that B10 found a significantly smaller peak-to-peak rotational light curve amplitude (0.6%), but their photometry was obtained one to two years earlier than our *Kepler* data.

The methodology described above makes approximations that depend on the fortuitous geometry wherein HAT-P-11b crosses nearly perpendicular to the stellar equator. Moreover, we also retained the approximation of neglecting stellar limb darkening. We believe that a more general formalism could be developed along the same line of reasoning, which could be applied to less strongly inclined planets, and could include realistic limb darkening. That generalization is beyond the scope of this paper, and we will utilize our current estimate of the total spot flux deficit of HAT-P-11 when interpreting our results in the next section.

## 8. RESULTS AND DISCUSSION

Our MCMC fits produce excellent agreement with the *Kepler* data (Figure 6). The retrieved parameters agree closely whether we solve for limb darkening or fix the coefficients at their Kurucz model atmosphere values. Moreover, the retrieved linear coefficient in the former case ($u = 0.626 \pm 0.014$, Table 1) is in excellent agreement with the model atmosphere value (0.6179). We conclude that the HAT-P-11 system parameters derived from the *Kepler* MCMC fits are robust, and not model-dependent via limb darkening. Knutson et al. (2007) reached a similar conclusion in their analysis of *HST* observations of HD 209458b.

The $\chi^2$ value for the best-fit solution shown in Figure 6 is 417 for the in-transit points, for 112 degrees of freedom. Thus, the error bars based purely on *Kepler* photometric precision must be increased by a factor of two to account for the imperfect precision of star spot removal. That factor was applied in the MCMC fits, as noted in Section 5.2.

Both the *J*-band and *B*-band transits imply linear limb-darkening coefficients ($u$ in Table 1) that are in reasonable agreement with model atmosphere values, but they do hint that limb darkening for the real star could vary more strongly with wavelength than the model atmosphere predicts. The MCMC posterior distribution for $u$ in the *B* band (not illustrated) peaks at unity, and values exceeding unity are unphysical. The one-sided Gaussian distribution has $\sigma = 0.080$, so our result (Table 1, $u = 1.000 \pm 0.080$) falls *above* the model atmosphere value (0.862) by $1.8\sigma$. The *J*-band result ($u = 0.086 \pm 0.065$) similarly falls *below* the model atmosphere value (0.244) by $2.4\sigma$. If discrepancies in model atmosphere predictions for $u$ do vary with wavelength in this fashion (stronger at short-λ, weaker at long-λ), we would not necessarily expect a significant effect in the *Kepler* band, because it lies intermediate in wavelength between our *B*- and *J*-band data. Moreover, any such systematic variation should be confirmed using transits of larger planets, exhibiting deeper transits, where greater precision in derived limb darkening can be achieved. We note that there is observational precedent for limb darkening at short wavelengths to be stronger than model atmosphere predictions (Tingley et al. 2006). We plan additional simultaneous *B*- and *J*-band observations of giant planet transits.

Our results for the *J*-band transit are inconsistent with the *Kepler* results as regards the planetary radius. In the *J* band, we find that $R_p/R_s$ is 6% larger than the *Kepler* solution (0.0627 versus 0.0589), and the difference is more than five times the precision of the *J*-band measurement. We regard the *Kepler* result as definitive, so we consider how this discrepancy can be explained.

One potential explanation of a discrepant radius in the *J* band is that it reflects a true variation of the planetary radius with wavelength due to atmospheric opacity. However, the difference here seems implausibly large, and we prefer a more mundane explanation. The transit of HAT-P-11b is relatively long in duration (2.3 hr) and shallow (0.004). Ground-based infrared photometry can be subject to baseline fluctuations caused by telluric water vapor absorption at the edges of the *JHK* bandpasses. The longer the duration of a transit event, the more sensitive it is to baseline effects, because the adopted baseline has to span a longer interval. Also, a given baseline error will have a greater relative effect for shallow transits. Hence, HAT-P-11 is particularly prone to baseline errors, and we regard the $R_p/R_s$ value from our *J*-band MCMC fits as unreliable at the level of accuracy needed for meaningful comparison with *Kepler* results. We note that the discrepancy would be even larger without the baseline correction that we applied in Section 2.2; evidently, our correction underestimates the telluric effects.

Although $R_p/R_s$ from our *J*-band data is questionable compared to the *Kepler* value, we believe that $a/R_s$ is reliable, and a useful complement to the *Kepler* results. As noted in Section 5.4, the *J*-band transit is sensitive to the total chord length. As already seen in Figure 1, the duration of the *J*-band transit predicted from the B10 discovery results (the blue curve in Figure 1) does not fit the transit duration seen in the *J*-band data. Unlike the situation with transit depth, the transit duration observed in the *J* band is insensitive to the telluric atmosphere. At this wavelength, the ingress and egress are sharp and well defined, and rapid changes of this type are much less likely to be caused by the telluric atmosphere. Fixing the orbital inclination at the *Kepler* value, our *J*-band fits give $a/R_s = 16.454 \pm 0.131$, in excellent agreement with the *Kepler* value of $16.549 \pm 0.230$. Transit determination of $a/R_s$ can be used to derive the stellar density (Seager & Mallen-Ornelas 2003) for comparison to asteroseismology results. However, the *Kepler* asteroseismology results for HAT-P-11 were regarded as preliminary by Christensen-Dalsgaard et al. (2010), so the comparison is premature.

We adopt our *Kepler*-1 solution (see Table 1) for the system parameters, and note that the stellar mass ($0.809\,M_\odot$) is well determined from the *Hipparcos* parallax and the isochrone fits performed by B10. This yields $R_s = 0.683\,R_\odot \pm 0.009\,R_\odot$, a $3.3\sigma$ revision from the B10 value ($0.752\,R_\odot \pm 0.021\,R_\odot$). Using our $R_p/R_s = 0.05892 \pm 0.00027$ yields $R_p = 4.39\,R_\oplus \pm 0.06\,R_\oplus$, a $2.1\sigma$ revision from B10 ($R = 4.73 \pm 0.16\,R_\oplus$). However, the presence of unseen star spots will cause the planet to appear larger in the transit solutions by 1.76%, as discussed in Section 7. We thus correct our radius for the planet downward to $R_p = 4.31\,R_\oplus \pm 0.06\,R_\oplus$. Hence, we find that both the planet and star are smaller than the B10 discovery values, at about the $3\sigma$ level.

We have been able to improve the system parameters of HAT-P-11 over the very thorough analysis by B10, in large part due to the numerous precise *Kepler* transits. These data have allowed us to remove the effect of star spot crossings,

resulting in a deeper transit. Although the deeper transit would tend to produce a larger planet, we also find a smaller star and that the decrease in stellar size, combined with our correction for uncrossed star spots, results in a smaller planet compared to B10. Also, in comparison to B10, we find a longer transit duration, and a smaller impact parameter since our orbital inclination is closer to 90°.

Our revised radius for HAT-P-11b has noteworthy implications for its internal structure. A mass–radius diagram for planets similar to HAT-P-11b is illustrated by Lissauer et al. (2011, their Figure 5). The H–He envelope mass implied by the previous radius of HAT-P-11b is close to 20%; our new radius reduces the required envelope mass to about 14%, very close to the envelopes implied for GJ 436b and *Kepler*-4b.

The radius of HAT-P-11b is now known with sufficient precision to contemplate useful comparisons with other spaceborne transit observations such as those that *HST* and *Spitzer* could acquire. These comparisons could potentially reveal an atmospheric signature of HAT-P-11b. Moreover, we point out that long-term monitoring of the system by *Kepler*, potentially supported by precise ground-based photometry after *Kepler* has ended, could reveal fundamental information on the magnetic cycle of the star. Because the planet transits nearly perpendicular to stellar active latitudes, monitoring of the number and orbital phase of star spot crossings could allow us to construct a stellar 'Butterfly diagram' depicting the cyclic evolution of magnetic eruptions at the stellar photosphere of this active K-dwarf star.

While this paper was under review, two additional analyses of HAT-P-11b based on the *Kepler* data were announced. Southworth (2011) obtains system parameters that agree with our Table 1. He does not explicitly correct for the effect of star spots, instead treating the spot perturbations as correlated errors. An analysis by Sanchis-Ojeda & Winn (2011) also finds similar system parameters as per our Table 1. These authors correct for crossed spots "by hand," but do not correct the planetary radius for the effect of uncrossed spots. Interestingly, Sanchis-Ojeda & Winn (2011) also discuss a second possible orientation for the system in which the star is viewed nearly pole-on. In that orientation, the two preferred phases of star spot crossings could be caused by one active band of spots encircling the stellar pole. While we cannot rigorously exclude that geometry, we note that our correction for uncrossed spots (Section 7)—based on viewing the star as per the Figure 8 geometry—predicts a peak-to-peak variation in the stellar rotational light curve of $\leqslant 1.76\%$, in good agreement with the variability seen in the *Kepler* data ($\sim 1.5\%$). That agreement would have to be accidental if the star is being viewed pole-on, so we believe that our Figure 8 geometry is correct, and the stellar pole is nearly in the plane of the sky.

We thank Dick Joyce for his expert assistance with FLAMINGOS, and we thank the anonymous referee for insightful comments that allowed us to improve this paper. Eric Agol acknowledges support from NSF Career grant AST-0645416.

## REFERENCES

Alonso, R., Barbieri, M., Rabus, M., et al. 2008, A&A, 487, L5
Bakos, G. A., Torres, G., Pál, A., et al. 2010, ApJ, 710, 1724
Baraffe, I., Chabrier, G., & Barman, T. 2008, A&A, 482, 315
Bean, J., Kempton, E. M.-R., & Homeier, D. 2010, Nature, 468, 669
Borucki, W. J., Koch, D., Basri, G., et al. 2010, Science, 327, 977
Charbonneau, D., Allen, L. E., Megeath, S. T., et al. 2005, ApJ, 626, 523
Christensen-Dalsgaard, J., Kjeldsen, H., Brown, T. M., et al. 2010, ApJ, 713, L164
Claret, A., Diaz-Cordoves, J., & Gimenez, A. 1995, A&AS, 114, 247
Colon, N. D., & Ford, E. B. 2009, ApJ, 703, 1086
Croll, B., Lafreniere, D. L., Albert, L., et al. 2011, AJ, 141, 30
Czesla, S., Huber, K. F., Wolter, U., Schroter, S., & Schmitt, J. H. M. M. 2009, A&A, 505, 1277
Deming, D., Seager, S., Richardson, L. J., & Harrington, J. 2005, Nature, 434, 740
Desert, J.-M., Bean, J., Miller-Ricci Kempton, E., et al. 2011, ApJ, 731, L40
Dittmann, J. A., Close, L. M., Green, E. M., Scuderi, L. J., & Males, J. R. 2009, ApJ, 699, L48
Eastman, J., Siverd, R., & Gaudi, B. S. 2010, PASP, 122, 935
Elston, R. 1998, Proc. SPIE, 3354, 404
Ford, E. B. 2005, AJ, 129, 1706
Gilliland, R. L., Jenkins, J. M., Borucki, W. J., et al. 2010, ApJ, 713, L160
Hirano, T., Narita, N., Shporer, A., et al. 2011, PASJ, 63, 531
Kipping, D. M. 2010, MNRAS, 408, 1758
Kipping, D. M., & Bakos, G. A. 2011, ApJ, 733, 36
Knutson, H. A., Charbonneau, D., Noyes, R. W., Brown, T. M., & Gilliland, R. L. 2007, ApJ, 655, 564
Lissauer, J. J., Fabrycky, D. C., Ford, E. B., et al. 2011, Nature, 470, 53
Mandel, K., & Agol, E. 2002, ApJ, 580, L171
Pont, F., Gilliland, R. L., Knutson, H., Holman, M., & Charbonneau, D. 2009, MNRAS, 393, L6
Pont, F., Zucker, S., & Queloz, D. 2006, MNRAS, 373, 231
Sada, P., Deming, D., Jackson, B., et al. 2010, ApJ, 720, L215
Sanchis-Ojeda, R., & Winn, J. N. 2011, ApJ, in press
Seager, S., & Mallen-Ornelas, G. 2003, ApJ, 585, 1038
Sing, D. K. 2010, A&A, 510, A21
Southworth, J. 2008, MNRAS, 386, 1644
Southworth, J. 2011, MNRAS, in press (arXiv:1107.1235)
Tingley, B., Thurl, C., & Sackett, P. 2006, A&A, 445, L27
Waite, I. A., Marsden, S. C., Carter, B. D., et al. 2011, MNRAS, 413, 1949
Walkowicz, L. M., Basri, G., Batalha, N., et al. 2011, AJ, 141, 50
Winn, J. N., Johnson, J. A., Howard, A. W., et al. 2010, ApJ, 723, L223